Identification of weakly- to strongly-turbulent three-wave processes in a micro-scale system (supplemental information)

J. Orosco, W. Connacher, and J. Friend*
Medically Advanced Devices Laboratory, Center for Medical Devices
Department of Mechanical and Aerospace Engineering University of California San Diego, La Jolla, CA 92093-0411 USA
(Dated: April 22, 2022)

I. WAVE TURBULENCE REGIME CLASSIFICATION PARAMETERS

In deducing a metric for classifying wave turbulent regimes, we take an approach similar to that described by Zakharov [1] and L'vov and Nazarenko [2]. Their techniques involve an intuitive comparison of the nonlinear resonance broadening (NRB), δ_{NRB}, to the spacing in the eigenmode grid that is imposed by the finite geometry, δ_ω. When $\delta_{\mathrm{NRB}} \ll \delta_\omega$, the wavemode character will be dominated by discrete wave turbulence (DWT). When $\delta_{\mathrm{NRB}} \gg \delta_\omega$, the wavemode character will be dominated by kinetic wave turbulence (KWT). Otherwise, the characteristics of both types may be observed, a scenario referred to as mesoscopic wave turbulence (MWT) though we call it intermediate WT (IWT).

The eigenmode grid spacing at a particular wavenumber κ is found in terms of the smallest possible wave number, $k_m = \pi/L$, as

$$\begin{aligned} \delta_k/k_m &\approx d\omega/dk, \\ \Rightarrow \delta_\kappa &\approx k_m \left.\frac{d\omega}{dk}\right|_{k=\kappa}, \end{aligned} \tag{1}$$

for a container of width L and where we have assumed homogeneous Dirichlet boundaries. The form of the dispersion relation, $\omega_k = \omega(k)$, depends on the particular system. In this note, we consider both shallow and deep water capillary waves. We distinguish between these with the inverse capillary length, $k_* = \sqrt{\rho\, g/\sigma}$, and fluid depth, h. If $k_* \ll k \ll 1/h$, the conditions are shallow. If $k \gg 1/h$, the conditions are deep [3].

The NRB is given as [2]

$$\delta_{\mathrm{NRB}} = \begin{cases} |V_k\, a_k|\, \mathcal{N}_k, & (\mathrm{DWT}) \\ |V_k|^2 |a_k|^2 (k\,L)^2/\omega_k, & (\mathrm{KWT}) \end{cases} \tag{2}$$

where $|(\,\cdot\,)|$ denotes the complex modulus. The parameter V_k is an interaction coefficient that arises in the collision integral from kinetic wave theory. The amplitude variable a_k is the canonical transform of the orthonormal Fourier amplitude, ζ_k, that diagonalizes a corresponding Hamiltonian [4]:

$$\zeta_k = \sqrt{\frac{\rho\,\omega_k}{2\,\sigma\,k^2}}(a_k + a^*_{-k}), \tag{3}$$

where σ is the interfacial tension and ρ is the fluid density. Note that eqn. (3) assumes normalization of the Fourier transform by $\sqrt{2\,\pi}$. Here $\mathcal{N}_k$ is the number of exact resonances that are dynamically relevant. For the capillary wave systems we consider here, waveumber locality is assumed—$k_1 \sim k_2 \sim k_3$—so that $\mathcal{N}_k \gtrsim 1$. We set $\mathcal{N}_k = 1$ for our order-of-magnitude analysis in order to avoid unnecessary complexity.

A. Shallow regime parameters ($k_* \ll k \ll 1/h$)

The shallow water capillary wave dispersion relation is

$$\omega_k^2 = \frac{\sigma\, h}{\rho} k^2. \tag{4}$$

The interaction coefficient for shallow water waves is [3]:

$$V_k = \frac{k^2}{8\,\pi}\left(\frac{\sigma}{4\,\rho\,h}\right)^{1/4}. \tag{5}$$

Combining eqns. (1)–(5), along with the respective requirements on δ_{NRB} and δ_ω, we arrive at the shallow-water conditions

$$\mathrm{DWT} \quad \text{if} \quad \Delta_s = \tfrac{1}{16\,\pi}\mathcal{A}_c/\mathcal{A}_w \ll 1, \tag{6a}$$
$$\mathrm{KWT} \quad \text{if} \quad \Lambda_s = 2\,\pi^2\,\mathcal{S}_w\,\Delta_s^2 \gg 1, \tag{6b}$$
$$\mathrm{MWT} \quad \text{otherwise}. \tag{6c}$$

The value $\mathcal{A}_w = 1/k\,\zeta_k$ is the aspect ratio of the wave and $\mathcal{A}_c = 1/k_m\,h$ is the aspect ratio of the container. The wave seclusion is $\mathcal{S}_w = k/k_m$, with $\mathcal{S}_w \gg 1$ indicating a wave that is essentially unaffected by the boundaries. Thus, the condition for DWT in the shallow water case is that the container geometry should be much less shallow than the wave geometry. And for KWT, the opposite condition is weakly required in concert with a wave that is sufficiently isolated from boundary effects.

B. Deep regime parameters ($k \gg 1/h$)

The deep water capillary wave dispersion relation is

$$\omega_k^2 = \frac{\sigma}{\rho} k^3. \tag{7}$$

By pairing the wavenumber locality assumption with an order-of-magnitude analysis, the interaction coefficient for deep water [4] is reduced to

$$V_k = \frac{1}{8\,\pi}\sqrt{\frac{\rho\,\omega_k^3}{2\,\sigma}}. \tag{8}$$

Combining eqns. (1)–(8), along with the respective requirements on δ_{NRB} and δ_ω, we arrive at the deep-water conditions

$$\text{DWT} \quad \text{if} \quad \Delta_d = \tfrac{1}{12\,\pi}\mathcal{S}_w/\mathcal{A}_w \ll 1, \tag{9a}$$
$$\text{KWT} \quad \text{if} \quad \Lambda_d = \tfrac{3\,\pi^2}{2}\mathcal{S}_w\,\Delta_d^2 \gg 1, \tag{9b}$$
$$\text{MWT} \quad \text{otherwise.} \tag{9c}$$

As expected, in shallow water, the discreteness depends on both container dimensions, whereas in deep conditions, only the lateral dimension is relevant. Equations (9) establish requirements for the wave steepness relative to the breadth of the domain in deep water. In this case, the kinetic condition weakly requires wave seclusion while carrying a somewhat stronger requirement of wave steepness. This result qualitatively agrees with expressions that can be found elsewhere in the literature for deep water gravity waves [5, 6].

C. Intermediate regime exactly interpolated parameters ($k \sim 1/h$)

In intermediate regimes, where the capillary wavelength is of the order of the depth of the basin, the governing theory does not have a simple reduced expression. We address this complication with polynomial interpolation in log-log space. Since these expressions are linear in log-log space, we only need to fulfill two conditions at each endpoint—slope and magnitude—in order for the interpolation to be exact. This is achieved with the quartic polynomial:

$$y = a_3\,x^3 + a_2\,x^2 + a_1\,x + a_0, \tag{10}$$

where $x = \log_{10}(k)$ and $y = \log_{10}(\zeta_i(k))$ for the intermediate discrete bound Δ_i (we will use the discrete bound as an example and note that the kinetic bound is handled in precisely the same manner).

The coefficients are found by solving a system of equations satisfying the boundary conditions. Let $x_s = \log_{10}(k_s)$ and $x_d = \log_{10}(k_d)$, where k_s and k_d are the shallow and deep wavenumber bounds, respectively. Let $y_s = \log_{10}(\widehat{\zeta}_s(k_s))$ and $y_d = \log_{10}(\widehat{\zeta}_d(k_d))$. The terms ζ_s and ζ_d are obtained by rewriting the corresponding Δ expression in terms of Fourier transformed surface height. Then the interpolating polynomial coefficients are obtained by solving

$$\begin{bmatrix} x_s^3 & x_s^2 & x_s & 1 \\ x_d^3 & x_d^2 & x_d & 1 \\ 3\,x_s^2 & 2\,x_s & 1 & 0 \\ 3\,x_d^2 & 2\,x_d & 1 & 0 \end{bmatrix} \begin{bmatrix} a_3 \\ a_2 \\ a_1 \\ a_0 \end{bmatrix} = \begin{bmatrix} y_s \\ y_d \\ \gamma_s \\ \gamma_d \end{bmatrix}, \tag{11}$$

where $\gamma_s = -1$ and $\gamma_d = -2$ are the power-laws satisfied by ζ_s and ζ_d, respectively, for the discrete bound. The interpolated bound is then $\zeta_i = 10^y$, with y obtained from eqn. (10). The top two rows in eqn. (11) correspond to the amplitude constraints, while the bottom two rows correspond to the slope constraints. Note that this interpolation is exact and completely specified by Δ_s and Δ_d. The full piecewise boundary definitions are infinitely differentiable for all wavenumbers.

When evaluating expressions such as $\chi_h \gg 1$ and $\chi_l \ll 1$, we set $\chi_h \geq \theta$ and $\chi_l \leq 1/\theta$, where $\theta \gg 1$ is a dimensionless tolerancing variable. Its value is chosen large enough so that there exists a well-defined mesoscopic gap [2], but not so large that the conditions for DWT and/or KWT are more severe than evidenced by the observations. As it turns out, an intuitive physical definition that also satisfies these criteria is the value of θ that causes the bounds to cross at the end of the turbulent cascade. This means that the bounds have meaning up to the end of the cascade, but not beyond. For the present system, this happens when $\theta \approx 5\,\pi$.

Thus, for example, $\Delta_s \ll 1$ becomes $\Delta_s < 1/\theta$ and can be rearranged: $\widehat{\zeta}_s(k) < (16\,\pi\,h\,k_m)/(\theta\,k)$ for $k \leq k_s$. So that $\gamma_s = -1$ and $y_s = \log_{10}((16\,\pi\,h\,k_m)/(\theta\,k_s))$.

II. WAVELET-BASED BISPECTRUM AND BICOHERENCE

Wavelet transforms of the time-dependent surface data, $\zeta(t) \mapsto \widetilde{\zeta}(t, f)$, were implemented in this work using Python v 3.8.12 along with the PyWavelets module v 1.1.1. The continuous wavelet transform ('cwt') was performed using a complex Gaussian first derivative ('cgau1') wavelet, following the work of van Milligen [7] in the development of the wavelet-based bicoherence as an improvement over Fourier methods.

The bicoherence is

$$b_{n,m} = \frac{|\langle\widetilde{\zeta}(t, f_n)\,\widetilde{\zeta}(t, f_m)\,\widetilde{\zeta}^*(t, f_n + f_m)\rangle_t|}{\langle|\widetilde{\zeta}(t, f_n)\,\widetilde{\zeta}(t, f_m)\,\widetilde{\zeta}^*(t, f_n + f_m)|\rangle_t}. \tag{12}$$

The difference between the numerator and denominator is order of operations of the time average $\langle\,\cdot\,\rangle_t$ and the modulus $|\,\cdot\,|$. The numerator is called the bispectrum. In the bispectrum, phase information is removed after taking the time average, so that this describes average three-wave coupling strength at a particular point in frequency space. An example of the bispectrum for data taken at 125 mW (the margin between KWT and SWT)

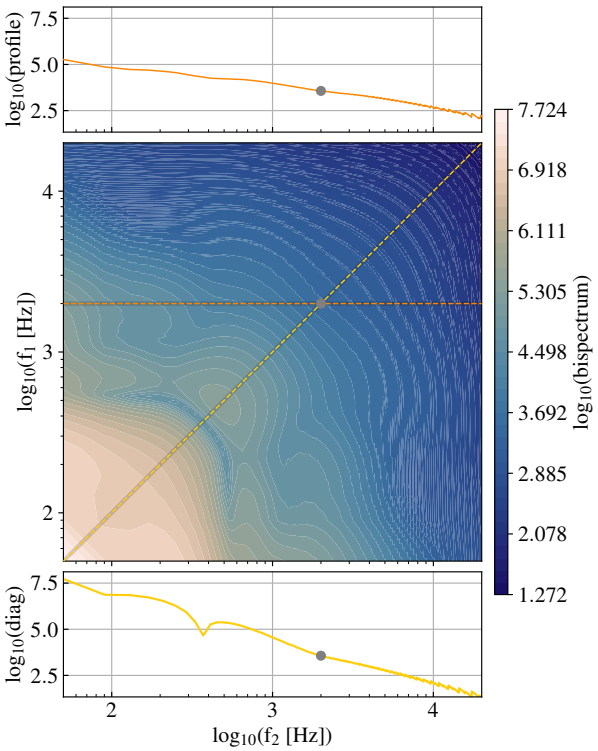

FIG. 1. Bispectrum of interfacial capillary wave dynamics at an input of 125 mW.

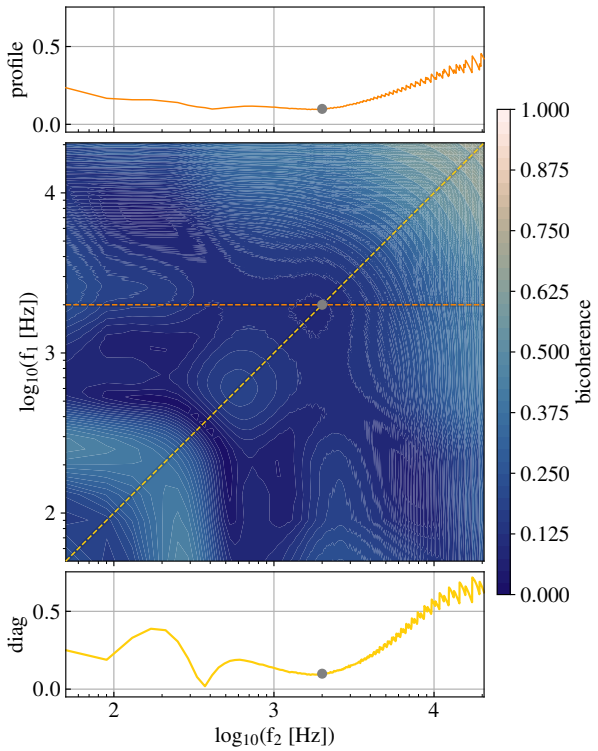

FIG. 2. Bicoherence of interfacial capillary wave dynamics at an input of 125 mW.

is provided in Fig. 1. In the denominator of eqn. (12), phases are all set to zero (*i.e.*, made equivalent) before taking the time average, which amounts to perfect phase coupling. Thus, bicoherence, $b \in [0, 1]$, is a measure of the three-wave coupling strength, and is therefore relevant for analysis of capillary waves specifically. An example of the bicoherence for data taken at 125 mW is provided in Fig. 2.

III. HIGH-SPEED DIGITAL HOLOGRAPHIC MICROSCOPY

The center of the air-water interface was imaged using high-speed digital holographic microscopy (DHM, Lynceé Tec SA, Lausanne, Switzerland). The DHM system is configured to record holograms with a high-speed camera (Nova S12, Photron, San Diego, California, USA) using a 10x, 0.3 NA objective (Leica Microsystems Inc., Buffalo Grove, Illinois, USA). Imaging configuration and hologram acquisition were facilitated by proprietary software (Koala v 8.1, Lynceé Tec SA, Lausanne, Switzerland). We obtained surface holograms covering a 300 µm x 300 µm square central region of the oscillating fluid interface. Holograms were recorded at 115.2 kfps and had a face-normal resolution of roughly 10 nm and a 1.2 µm image plane resolution.

IV. DEVICE FABRICATION AND CHARACTERIZATION

The device consists of three major elements: (i) the piezoelectric transducer substrate, (ii) metallic electrodes, and (iii) a polyimide annulus. The piezoelectric transducer was a 25 mm x 20 mm x 0.5 mm single-crystal lithium niobate substrate, diced from a 4 in. wafer (Precision Micro-Optics LLC, Burlington, Massachusetts, USA), in the 128° YX orientation, polished on both sides for face-normal transparency. Electrodes were deposited on each face of the wafer in two stages prior to dicing. First, a thin chromium layer of 20 nm was deposited for improved adhesion, and, subsequently, a 400 nm layer of gold was deposited (Discovery 18 Sputtering System, Denton Vacuum LLC, Moorestown, New Jersey, USA). Prior to deposition, a pattern of 6.35 mm diameter, 60 µm thick polyimide tape circles (CS Hyde Company, Lake Villa, Illinois, USA) was affixed to each side and aligned so that after deposition the tape could be removed from each side leaving a circular transparent window pattern. An annulus was then fabricated by cutting a 9.5 mm diameter circular hole into a 12.7 mm diameter, 60 µm thick polyimide tape circle (CS Hyde Company, Lake Villa, Illinois, USA). The annulus was affixed to the top face, encircling the transparent win-

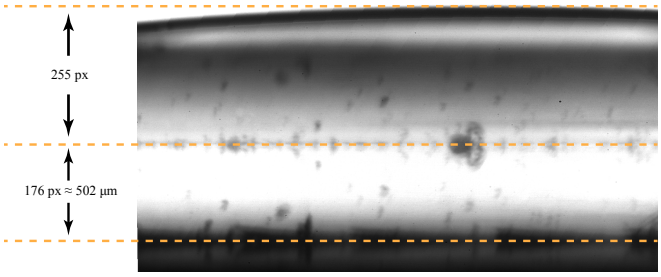

FIG. 3. The portion in the bottom of the image (between dashed lines) corresponds to the transducer. The top portion (between dashed lines) corresponds to the fluid volume. Pixel comparison yields a maximum quiescent fluid volume height of approximately 725 µm.

dow. A 40 µL volume of water was then pipetted into the annulus, producing a maximum fluid height of ≈ 725 µm.

The fluid height was measured by taking profile images of the quiescent fluid volume in the device. The device thickness was measured with a precision electronic micrometer (54-860-001-1, Fowler High Precision Inc., Canton, Massachusetts, USA) and found to be 502 µm. The profile image was captured with a digital camera (Fastcam Mini UX, Photron, San Diego, California, USA). The estimate of 725 µm (see Fig. 3) for the fluid height was determined by comparing the number of pixels occupied by the 502 µm-thick substrate, 176, to the number of pixels occupied by the fluid column, 255.

The device used in this study was constructed to loosely approximate the dimensions of surface-wetting "puddles" that form on the planar working surface of high-frequency (MHz+) portable ultrasonic nebulizers developed in our lab. An example of such a device can be found in Ref. [8]. We have also separately included a video file, 'atomizing_fluid.mp4', that demonstrates atomization from the surface of a similarly constructed transducer substrate. Some examples of fluid volume geometry can be found in the included image file 'varied_geometry.pdf'.

In Table I, we provide measurements of the substrate vibration displacement amplitude, ξ_p, and particle velocity, $\dot{\xi}_p$, made from 0 to 350 mW input power. The measurements were obtained with a laser Doppler vibrometer (UHF-120, Polytec Inc., Irvine, California, USA). The dependence of the particle velocity on the input power has long been known to be quadratic in these devices [9]. In Fig. 4, we provide a plot of these measurements along with a linear least squares fit of the data to the function $\dot{\xi}_p = 1.71\sqrt{P}$, indicating a good fit with the correlation coefficient $R^2 = 0.9879$.

TABLE I. Calibration measurements for substrate displacement amplitude, ξ_p, and substrate particle velocity, $\dot{\xi}_p$, as a function of input power, and categorized according to the type of wave turbulence it produces in our system. The parameters are related as $\dot{\xi}_p = 2\,\pi\,f\,\xi_p$, where $f = 7.001$ MHz is the resonant frequency of the device.

Turb. type	Input power [mW]	ξ_p [nm]	$\dot{\xi}_p$ [cm/s]
Quiescent	0	0	0
	1.05	0.17	0.76
	2.65	0.33	1.5
DWT	5.50	0.55	2.4
IWT	12.5	1.45	6.36
KWT	54.0	2.75	12.1
	125.	4.13	18.2
SWT	200.	5.71	25.1
	250.	6.29	27.7
	300.	6.71	29.5
	350.	7.27	32.0

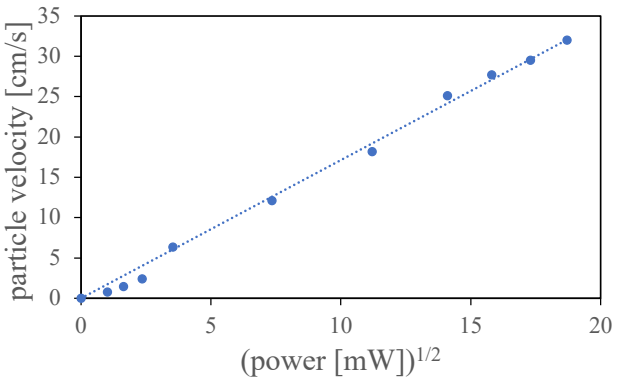

FIG. 4. The particle velocity depends upon the square root of the input power such that $\dot{\xi}_p = 1.71\sqrt{P}$.

* Corresponding author: jfriend@ucsd.edu

[1] V. Zakharov, Eur. J. Mech. B-Fluids Three-Dimensional Aspects of Air-Sea Interaction, **18**, 327 (1999).
[2] V. S. L'vov and S. Nazarenko, Phys. Rev. E **82**, 056322 (2010).
[3] V. E. Zakharov, V. S. L'vov, and G. Falkovich, *Kolmogorov Spectra of Turbulence I: Wave Turbulence*, 1st ed., Springer Series in Nonlinear Dynamics (Springer, Berlin, Heidelberg, 1992).
[4] A. N. Pushkarev and V. E. Zakharov, Physica D **135**, 98 (2000).
[5] S. Nazarenko, J. Stat. Mech. **2006**, L02002 (2006).
[6] P. Denissenko, S. Lukaschuk, and S. Nazarenko, Phys. Rev. Lett. **99**, 014501 (2007).
[7] B. P. van Milligen, C. Hidalgo, and E. Sánchez, Phys. Rev.

Lett. **74**, 395 (1995).
[8] A. Huang, W. Connacher, M. Stambaugh, N. Zhang, S. Zhang, J. Mei, A. Jain, S. Alluri, V. Leung, A. E. Rajapaksa, and J. Friend, Lab Chip **21**, 1352 (2021).
[9] A. R. Rezk, L. Y. Yeo, and J. R. Friend, Langmuir **30**, 11243 (2014).